Biodegradable shape memory polymer: Surface crystal effect on osteochondral regeneration

Suji Park

Department of Medical Device Industry

The Graduate School, Yonsei University

Biodegradable shape memory polymer: Surface crystal effect on osteochondral regeneration

Directed by Professor Hak-Joon Sung

The Master's Thesis

Submitted to the Department of Medical Device Industry,

the Graduate School of Yonsei University

in partial fulfillment of the requirements for the degree of

Master of Medical Science

Suji Park

December 2023

This certifies that the Master's Thesis
of Suji Park is approved.

_____

Thesis Supervisor: Hak-Joon Sung

_____

Thesis Committee Member#1: Kang Suk lee

_____

Thesis Committee Member#2: Kyubae Lee

The Graduate School
Yonsei University

December 2023

ACKNOWLEDGMENTS

2 년의 시간이 지나 어느새 석사과정을 끝내고 졸업을 맞기 위해 학위 논문을 제출하게 되었습니다. 2 년이라는 대학원에서의 배움의 시간 동안 저에게 도움과 가르침을 주셨던 많은 분들께 짧은 지면으로는 부족하지만 감사 인사를 전하려 합니다. 우선, 턱없이 부족했던 저를 믿어 주시고 가르침을 주시면서 성장할 수 있도록 엄하지만 따뜻하게 이끌어 주셨던 지도 교수님, 성학준 교수님께 진심으로 깊은 감사의 마음을 전합니다. 또한, 석사 과정 동안 함께 연구를 진행하면서 학문적으로 가르침을 주시며 많은 조언을 아끼지 않으시고 바쁜 와중에도 논문 심사를 위한 시간을 내어 주신 이규배 박사님과 이강석 박사님께도 진심으로 감사드립니다. 대학원 생활을 시작할 때부터 저를 지켜봐 주시고, 무사히 끝마칠 수 있도록 가르침과 조언을

아끼지 않은 재생 의공학 연구실 식구들에게도 진심으로 감사함을 전합니다.

그리고 학위 과정 동안 응원을 아끼지 않고 2 년간의 행복과 슬픔을 같이 겪어준 내 친구 승희, 늘 곁에서 격려와 웃음을 같이 주던 친구들 미영이, 서현이, 수정이, 지원이, 하은이 2년 동안 많은 힘이 되어 고마움을 전합니다.

마지막으로, 길었던 배움의 시간 동안 묵묵히 저의 뒤에서 응원해주시고 지원을 아끼지 않으면서 지켜봐 주신 우리 엄마, 아빠께 깊이 감사드립니다. 그리고 늘 말없이 응원해주고 곁에서 도움을 주었던 제 동생 현수에게도 고마움을 전합니다.

TABLE OF CONTENTS

LIST OF FIGURES

LIST OF TABLES

ABSTRACT

Biodegradable shape memory polymer: Surface crystal effect on osteochondral regeneration

Suji Park

Department of Medical Device Industry,

The Graduate School of Yonsei University

(Directed by Professor Hak-Joon Sung)

In tissue engineering and regenerative medicine, there is a growing demand for innovative strategies that can address the complex and dynamic needs of repairing both bone and cartilage tissues. To mimic environment of osteogenesis and chondrogenesis, crystallinity of polymer surface that cells are attached is important because it regulates interactions between cells and surfaces. For controlling interactions, Shape Memory Polymer (SMP) and thiol-functionalized hydroxyapatite nanoparticles (HANPs) are conjugated and crystalline structures of HANPs act as nucleation agents and stimulate aggregation of crystal ("crystal-packing") around the HANPs particles. As the crystal growing, cell-cell interactions are hindered, simultaneously, cell-surface interactions are enhanced for osteogenesis, in contrast, SMP surface induces cell-cell interactions for chondrogenesis relatively. And HANPs conjugated SMP (H-SMP) exhibits increased biodegradability compared to SMP. The enhanced biodegradability of H-SMP is suitable for bone regeneration speed, whereas the relatively slower degradation of SMP is suitable for cartilage regeneration speed. As a result, biodegradable SMP and H-SMP gradient 3D

porous scaffolds appears concurrent regeneration of bone and cartilage on rat's osteochondral defect model.

Keywords: Surface crystal structure, Bio-degradable, Shape-memory polymer, Osteochondral regeneration

Biodegradable shape memory polymer: Surface crystal effect on osteochondral regeneration

Suji Park

Department of Medical Device Industry,

The Graduate School of Yonsei University

(Directed by Professor Hak-Joon Sung)

I. INTRODUCTION

When tissues are defected and scaffolds are implanted for regeneration, cells infiltrate into scaffolds with contacting with surfaces of scaffolds. It was discovered that interactions between cells or cells and surfaces determine cell fate[1]. Mesenchymal stem cells (MSCs) are highly sensitive to surface cues, and their differentiation is influenced by these interactions. Cell-cell interactions induce cell aggregation[2] and cell-surface interactions promote cell spreading[3]. As widely known, cell aggregation induces chondrogenesis, while cell spreading promotes osteogenesis. Hence, the regulation of interactions between the surface to which cells are attached and the cells alters the environment in which cells grow. By using that differences in such interactions give rise to surface-dependent influences on the direction of differentiation, it is possible to create

conditions for simultaneously mimicking the environments conducive to both osteogenesis and chondrogenesis.

The regulation of interactions between cells and surfaces is influenced by changes in the surface topography[4]. To generate the environments of osteogenesis and chondrogenesis, it is necessary to regulate the crystallinity of surfaces in contact with cells for changing surface topography. To control interactions by changing crystalline structures, Shape Memory Polymer (SMP) and thiol-modified hydroxyapatite nanoparticles (HANPs) are conjugated.

SMP is semi-crystalline polymer[5] and HANPs are also polymers that have high degree of crystallinity. Owing to HANPs act as nucleation agents, simultaneous crystallization[6-8] and aggregation of crystals occur around the dispersed HANPs after cross-linking of SMP and HANPs. And it refers as crystal-packing. As the crystal grows, cell-cell interactions are disturbed physically because packed crystals act as barriers, impending cell-cell adhesion. In other words, cells with hindered cell-cell interactions experience an increased interaction with the surfaces, resulting in an expanded attachment area on the surface. Therefore, HANPs conjugated SMP (H-SMP) with enhanced cell-surface interactions induces osteogenesis, whereas SMP with relatively more cell-cell interactions induces chondrogenesis.

HANPs are biocompatible and biodegradable materials[9-11]. So, H-SMP is more biodegradable then SMP. To prevent the need for a secondary surgery for scaffold removal and to facilitate nutrient and oxygen supply[12], biodegradable 3D porous scaffolds are employed. The scaffold has bilayer with SMP and H-SMP for simultaneous

regeneration of bone and cartilage tissues utilizing the surface characteristics of SMP and H-SMP.

Since cartilage and bone tissues possess different mechanical and structural characteristics, research into treatment methods that address both simultaneously is actively underway. To regenerate both bone and cartilage tissues, various studies are being conducted, including the use of biodegradable polymers in porous 3D scaffolds, where segments for cartilage regeneration and bone regeneration are separately integrated into the tissues for regeneration.

Cartilage is a tissue with slow self-regeneration because of its low blood supply, and bone tissue typically takes 3-6 months for regeneration.[13, 14] Therefore, when degradation initiates in the H-SMP layer of the scaffold, the switch of space filling by new bone regeneration is supported, while in the SMP layer, degradation occurs relatively slowly, helping to support the duration of cartilage tissue regeneration and overall tissue regeneration. To prove this hypothesis, we created osteochondral defects in the rat's knee and then inserted the bilayer scaffold and histological analyses were conducted.

II. MATERIALS AND METHODS

1. Shape memory polymer (SMP) synthesis

All chemicals were purchased from Sigma-Aldrich (St. Louis, MO, USA). SMP was synthesized by ring-opening polymerization of ϵ-caprolactone (CL) and glycidyl methacrylate (GMA) monomers using an established protocol. Briefly, CL (94 mmol), 1,6-hexanediol initiator (0.5 mmol), and hydroquinone (0.6 mmol, 1:10 molar ratio of hydroquinone to GMA) as auto-crosslinking inhibitor were made to react in a three-necked round bottom flask, under stirring at 110 °C for 10 min, followed by the reaction of GMA (6 mmol) with the mixture for 10 min. Subsequently, 1,5,7-triazabicyclo[4.4.0]dec-5-ene (TBD, 0.5 mmol) was dissolved in acetonitrile solvent (2 mL) and was made to react at 110 °C for 6 h under a nitrogen atmosphere. The reaction mixture was dissolved in chloroform (30 mL) after cooling to room temperature (25 °C), and then, a white precipitate was formed in cold diethyl ether (800 mL, 4 °C). The final SMP product was obtained via vacuum drying (OV4-30, Jeio Tech, Daejeon, Republic of Korea) at room temperature.

2. Thiol-modification to Hydroxyapatite nanoparticles (HANPs)

The surface of Hydroxyapatite nanoparticle (HAp) was purchased from SkySpring Nanomaterials, Inc. (USA). HA nanoparticle was coated with (3-Mercaptopropyl) trimethoxysilane (MPTMS; Tokyo Chemical Industry Co., LTD., Japan) by a silanization reaction to obtain thiol functionalized HA nanoparticles. Dried HA nanoparticles were

accurately weighed HAp (6 g) was dispersed into 100 ml of ethanol, followed by the addition of 6 ml of MPTMS. The suspension was stirred for 48 h at 70 ℃. Modified HA nanoparticles was filtered and washed several times with deionized water and acetone to remove the excess unreacted MPTMS. Then thiol-modified hydroxyapatite nanoparticles (HANPs) was dried in oven at 60 ℃.

3. HANPs conjugated to SMP for fabrication of films and 3D porous scaffolds

PCL-PGMA powder was dissolved in N-methyl-2-pyrrolidone (NMP; Sigma-Aldrich, 1 $g \cdot ml^{-1}$) with 1% photo-initiator (Irgacure 2959, Sigma-Aldrich) for SMP group. And 10% HANPs powder was dissolved in NMP with PCL-PGMA and 1% photo-initiator for HANPs conjugated (H-SMP) group. The dissolved solution was poured on a slide glass and another slide glass covered it. Then, a UV lamp (300 to 400 nm, UVACUBE 400; Hoenle, Germany) was used to crosslink the solution for 200s for films. The 3D porous scaffolds were fabricated by porogen leaching technique. SMP and H-SMP solution was mixed with alginate beads with sizes in the range of 250-350 μm in a 1:2 weight ratio. After UV lamp crosslinked them, samples were soaked in 0.1M EDTA solution (HanLAB, Gyeonggi-do, Republic of Korea) to remove alginate beads.

4. Material characterization

The chemical structure of 94% PCL-co-06% PGMA with the molar ratio (%) was examined using 1H-NMR (400-MHz NMR, Avance III, Bruker Biospin, MD) spectra with chloroform-d ($CDCl_3$, Sigma-Aldrich) solvent. Also, Raman Spectrometer (LabRam Aramis, Horiba Jovin Yvon, Kyoto, Japan) confirmed successful grafting of thiol to HA nanoparticles.

The thermomechanical properties of films and 3D porous scaffolds were characterized by differential scanning calorimetry (DSC; Discovery DSC25, TA Instruments, New Castle, DE, USA), dynamic mechanical analysis (DMA; Discovery DMA850, TA Instruments, New Castle, DE, USA), and universal testing machine (UTM; 34SC-1, Instron, Norwood, MA, USA). First, Heat-flow-related thermal transitions were examined using DSC. The samples were heated to 150 °C, and then cooled to −80 °C for two cycles at a heating rate of 10 °C/min under a nitrogen atmosphere. The glass transition temperature (Tg), melting temperature (Tm), crystallization temperature (Tc), melting enthalpy (ΔHm), and crystallization enthalpy (ΔHc) were determined using the DSC thermograms. Next, DMA was used to determine Young's modulus in a strain-controlled mode with a rate of 5 mm·min^{-1} after incubation at 37 ℃ for 10 min. The compressive properties of 3D porous scaffolds (6mm×2mm) were characterized using a UTM at 37 °C. The samples compressed at a strain rate of 2mm/min-1 until the samples broken.

5. Shape memory test of SMP and H-SMP films

Films were examined its thermomechanical properties over four cycles (N) by dynamic mechanical analysis (DMA) in stress-controlled mode as follows. Samples [5 mm (W) × 5 mm (H) ×0.3 mm (D)] were heated to 55 °C, equilibrated for 10 min [original permanent shape; εp (0)], and then subject to shape programming by applying 50 kPa tensile stress at a rate of 4 kPa min −1. The samples were cooled to 0 °C at a rate of 2 °C min −1 and equilibrated for 10 min [maximum strain, ε1 (N)]. The tensile load was removed (5 kPa min −1) to yield a temporary shape [εu (N)], followed by heating to 55 °C at a rate of 2 °C min −1 to restore the permanent shape [εp (N)].

6. *In vitro* degradation test

3D porous scaffold punched with a diameter of 6mm and a thickness of 2mm ± 0.5mm, freeze-dried to remove the remaining water. Then, scaffolds were immersed in 1ml of a solution of HCl, NaOH and D.W mixed to adjust pH to 6 for accelerating a degradation speed. Because of inflammatory response that occurred when foreign materials were implanted to tissues. Then, Inflammatory cells lower the pH of the surrounding tissue to 6. So, to mimic the environment of inflamed tissue, scaffolds were soaked in solution adjusted to pH 6.

7. *In vivo* degradation test

To confirm biodegradability, dried 3D porous scaffolds that sterilized using EO gas were implanted in subcutaneous layer of back of BALB/C mice (Orient Inc.). At 60 days after implantation, mice were sacrificed using CO2 gas. Implanted tissues were fixed with 10% paraformaldehyde (Biosesang, Gyeonggi, Republic of Korea) for 4 days, embedded them in paraffin wax, and then sectioned the paraffin blocks to 5-μm-thick slices using a microtome (Leica Microsystems, Deerfield, IL, USA). Degradation of scaffolds were examined by hematoxylin and eosin (H&E) staining. Neo tissue formation area of stained tissues were examined with ImageJ (Fiji, National Institute of Health, MD, USA).

8. Polarized Optical Microscopy

SMP and H-SMP solution were poured on a slide glass and another one covered it. Then, UV-crosslinked films were dried in room temperature to remove solvent. Thin films were positioned between two polarized films (KENIS, Osaka, Japan) and crystal structure of surface of films was visualized by optical microscopy (Leica DMi8; Leica Microsystems, Wetzlar, Germany).

9. Atomic Force Microscopy

Atomic Force Microscopy (AFM; NX-10, Park Systems Corp., Gyeonggi-do, Republic of Korea) measured surface characteristics of SMP and H-SMP thin films with contact mode of AFM. Height of surface and roughness were measured from surface topography. Surface stiffness was confirmed with force-distance curve of AFM.

10. X-ray Diffraction (XRD)

The crystallographic characteristics of SMP/H-SMP films and HA-SH powders in the printed scaffolds were performed through HR-XRD (Rigaku, Tokyo, Japan) with diffraction angles (2θ) ranging from 0° to 90°.

11. Scanning Electron Microscope (SEM)

Cross-sectioned images of films were visualized by field-emission scanning electron microscope (FE-SEM; JEOL Ltd., Tokyo, Japan). Also, SEM-EDS analysis was performed for analysis of ion composition of films' surface.

12. Water contact angle

Water contact angle measurements on the surfaces of SMP and H-SMP films (thickness: 0.3 mm) were conducted using a Contact Angle Meter-2 (DSA 25; Kruss, Hamburg, Germany). A droplet (1-2 μl) of deionized water was applied, and the measurements were taken under ambient conditions (22-25 °C). The water contact angle and surface energy were measured within 5 s of applying the droplet. The analyses were performed using the software that accompanied the contact angle meter, which determined the angle at which the water droplet meets the film surface. This was achieved by fitting a tangent line or curve to the boundary of the droplet where it contacts the surface.

13. 2D cell morphology analysis

To confirm effects of surface topography to cells, hBMSCs (LONZA; passages 4 to 6, 3×103 cells/well) were cultured on the SMP/H-SMP films. After 24h, cells were rinsed with PBS 3 times and fixed with 4% paraformaldehyde (CellNest) for 10 min at room temperature. Actin was stained with Alexa fluor 488 conjugated phalloidin (1:200; Invitrogen, Waltham, MA, USA)) for 2h, and nuclei was stained with Hoechst 33342 (1:200; Thermo Fisher), followed by confocal imaging (LSM980; Zeiss, Oberkochen, Land Baden-Württemberg, Germany). Cell morphologies were analyzed by ImageJ (National Institute of Health). Also, to determine 2D cell adhesion ability using Cell Counting Kit-8 (CCK-8; Dojindo, Rockville, MD, USA) with absorbance readings at 450 nm in a microplate reader (BioTek, Winooski, VT, USA).

14. Immunocytochemistry

After culturing of hBMSC cells and spheroids, we rinsed them three times with PBS, and fixed them with 4% paraformaldehyde (CellNest, Gyeonggi, Republic of Korea) for 10~30 min at RT. We permeabilized the samples with 0.3% Tween 20 (Sigma-Aldrich) in PBS for 1 hour at RT and then blocked them with 0.3% Tween 20 and 3% bovine serum albumin (Millipore, MA, USA) for 1 hour at RT. We treated the samples with primary antibodies overnight at 4°C for analysis against tight junction marker [rabbit anti-ZO-1 (1:100; Invitrogen)], focal adhesion marker [mouse anti-Paxillin (1:500; Invitrogen)],

chondrogenesis markers [mouse anti-Col2 (1:200; Novus, CO) and rabbit anti-SOX9 (1:500; Millipore)] and osteogenesis markers [mouse anti-OCN (1:200; arigo Biolaboratories Corp., Taiwan) and rabbit anti-Col1 (1:200; Invitrogen)]. We then washed the samples and treated them with secondary antibodies in PBS for 2 hours at RT. The secondary antibodies used included anti-rabbit Alexa Fluor 488, anti-mouse Alexa Fluor 594 (the Jackson Laboratory, Bar Harbor, ME, USA). We counterstained the nuclei with Hoechst 33342 (1:200; Invitrogen), followed by confocal imaging (LSM980).

15. Spheroid production

To produce hBMSC spheroid, AggreWell 800 24-well culture plates (STEMCELL Technologies, Vancouver BC, Canada) were used after rinsing with an anti-adherent solution (STEMCELL Technologies) for 24 h, then hBMSC spheroids were produced by culturing on AggreWell plates (passages 4 to 6, 2.4 × 106 cells/well) for 24h.

16. Spheroid adhesion test

hBMSC spheroids (1.2 × 106 cells/well) were cultured on SMP/H-SMP films. After 3 days, spheroids were fixed with 4% paraformaldehyde (CellNest) for 30 min at room temperature. Actin and Nuclear were stained with Alexa fluor 488 conjugated phalloidin (1:200) and DAPI (Thermo Fisher). Confocal imaging (LSM980;) was performed to compare differences of morphologies of spheroids. Then, analysis of cell sprouting was

performed by ImageJ (National Institute of Health). We conducted spheroid adhesion ability test to determine quantitative differences using Cell Counting Kit-8 (CCK-8; Dojindo) with absorbance readings at 450 nm in a microplate reader (BioTek).

17. Differentiation of hBMSC spheroid

Spheroids (2.4 × 106 cells/well) were cultured for 3 weeks in Mesenchymal Stem Cell Chondrogenic/Osteogenic Differentiation Medium (Sciencell). Medium was changed every 2-3 days. After 3 weeks, spheroids were fixed with 4% paraformaldehyde (CellNest) for 30 min at room temperature. We determined expression of chondrogenesis and osteogenesis markers by immunocytochemistry.

18. qRT-PCR

Total RNA was extracted from spheroids using TRIzol reagent (Thermo Fisher Scientific), according to the manufacturer's protocol. The NanoDrop 2000 Spectrophotometer (Thermo Fisher) was used to quantify the RNA concentration by measuring A260. Complementary DNA (cDNA) was synthesized using AccuPower CycleScript RT Premix (Bioneer, Daejeon, Republic of Korea) and the T-100 Thermal Cycler (Bio-Rad, CA, USA) following the manufacturer's protocol. qRT-PCR was performed using the StepOne Plus RT PCR System (Applied Biosystems, MA, USA) using a primer (Table 1), cDNA, and SYBR Green PCR mix (Applied Biosystems),

followed by melting curve analysis. The result for each target gene was normalized to that of glyceraldehyde-3-phosphate dehydrogenase (GAPDH) and calculated using the comparative Ct ($2^{-\Delta\Delta Ct}$) values.

19. sulfated Glycosaminoglycan (sGAG) assay

To assess the content levels of sulfated Glycosaminoglycan sGAG in hBMSC spheroids during chondrogenesis, we determined the content of sGAG using a Blyscan kit (Biocolor, County Antrim, UK), respectively, following the manufacturer's instructions. Briefly, we chopped samples in a papain solution and heated them at 60°C for 6 hours. The absorbance was read at fluorescein wavelengths (excitation: 480 nm; emission, 520 nm) using a fluorescence microplate reader (Varioskan Flash 3001, Thermo Fisher Scientific). Next, the GAG content was quantified that 1,9-dimethylmethylene blue cationic dye binds to the sulfated GAG in lysate sample. The reaction product was centrifuged for 30 min at 14,000 rpm. After resuspension using a dye dissociation buffer, the absorbance was read at 656 nm using a colorimetric microplate reader.

20. Calcium deposition assay

As a functional indication of osteogenesis, we determined the intracellular calcium level of hBMSC spheroids using a QuantiChrom calcium assay kit (BioAssay Systems, Hayward, CA, USA), respectively, following the manufacturer's instruction. Briefly,

samples were harvested and dissolved in 0.5M hydrogen chloride (HCl; Sigma-Aldrich) solution at 60°C for overnight. The calcium was quantified in the way that phenolsulphonephthalein dye reacted with free calcium in lysate buffer for 3 min, followed by reading the optical density at 612 nm using a colorimetric microplate reader.

21. Animal study

The therapeutic effect of SMP/H-SMP 3D porous scaffold on cartilage and bone was validated in an osteochondral defect model of rat femur. To assess cartilage and bone tissue regeneration by 3D porous scaffolds, we made a medial parapatellar incision (1 cm) in the knee (n = 7 rats) and then laterally dislocated the patella to expose the articular cartilage. We created cylindrical defects (diameter, 2 mm; depth, 1.5 mm) using a motorized drill (diameter, 2 mm; Saeshin, Daegu, Republic of Korea). To avoid drilling heat-mediated denaturation of surrounding tissues, we irrigated them with saline (Daehan Pharmaceutical, Seoul, Republic of Korea) during the defecting process, which also removed tissue debris. The SMP scaffold was implanted within the cartilage layer and H-SMP scaffold was implanted within the bone layer. Also, an empty defect served as a control. We closed the soft tissue using 4-0 vicryl (Ethicon Inc., NJ, USA), followed skin suture using 4-0 black silk (Ailee Co. Ltd., Seoul, Republic of Korea).

After an 8-week implantation, rats were sacrificed using CO2 gas. We harvested, dissected, and fixed femurs in 10% paraformaldehyde (Biosesang) for 1 day. To examine

bone regeneration in the fixed femurs, we used μ-CT (Quantum GX2 microCT imaging system, PerkinElmer, Waltham, MA, USA).

22. Histological analysis

We treated the fixed femurs with a decalcifying solution-lite (Sigma-Al drich), embedded them in paraffin wax, and then sectioned the paraffin blocks to 5-μm-thick slices using a microtome (Leica Microsystems, Deerfield, IL, USA). We purchased all the staining reagents from Sigma-Aldrich. We subjected the slices to hydration for von-kossa or H&E staining by following standard protocols. In addition, we subjected the hydrated paraffin sections to safranin- O staining (0.1%, w/v) for 5 min after sequential treatment with hematoxylin for 5 min, fast green (0.1%, w/v) for 3 min, and acetic acid (1%, w/v) for 5 s. We used optical microscopy (Leica DMi8, Leica Microsystems) to image all stained slides.

To determine protein marker expression of chondrogenesis and osteogenesis in the hydrated slices with blocking, we conducted immunostaining with the overnight treatment of rabbit anti-aggrecan (1:100; Abcam, Cambridge, UK) with mouse anti-Col2 (1:100; Novus), or rabbit anti-Col1 (1:200; Thermo Fisher) with mouse anti-OCN (1:200; arigo Biolaboratories) at 4°C. We incubated the slices with the secondary antibodies for 2 hours at RT. Then, we counterstained nuclei with Hoechst 33342 (1:200; Invitrogen), followed by confocal imaging (LSM980).

23. Statistical analysis

Statistical analysis was conducted using one-way analysis of variance (ANOVA) with post hoc Bonferroni's and Tukey's analyses using SigmaPlot (version 12.0, Systat

Software, CA, USA). All data are presented as mean ± SD. The P values and sizes of the samples per group are denoted in each figure legend.

Table 1. PCR primer list

	Accession number	Primer sequence (5'-3')
GAPDH	NM_001256799.3	F-GTCAAGGCTGAGAACGGGAA R-AAATGAGCCCCAGCCTTCTC
SOX9	NM_000346.4	F-GACTTCCGCGACGTGGAC R-GACTTCCGCGACGTG GAC
Col2a1	NM_000089.4	F-GAGCCAAAGGATCTGCTGGT R-TTGGGGCCTTGTTCACCTTT
Aggrecan	NM_001135.3	F-AAGCAGGCTATGAGCAGTGT R-TCCCCCTCAAGTCTGTCTACAA
RUNX2	NM_001015051.4	F-TTACTTACACCCCGCCAGTC R-TATGGAGTGCTGCTGGTCTG
Cola1	NM_000088.4	F-CCCCTGGAAAGAATGGAGATG R-TCCAAACCACTGAAACCTCTG

OCN	NM_199173.6	F-GGGGCTACCTGTATCAAT GG R-TCAGCCAACTCGTCACAGTC

III. Results

1. Material characterization of SMP and SMP with thiol-modified hydroxyapatite nanoparticles (H-SMP)

The process of osteochondral tissue regeneration through surface crystal structure changes of shape memory polymers with enhanced biodegradability has been depicted in the scheme (**Fig.1**). As a first step to make differences of Shape memory polymer (SMP) surface, HANPs should be modified to crosslink with SMP. To make cross-linking segments between SMP and HANPs, we generate thiol-modified HANPs[15]. Thiol reacts with methacrylate of SMP by generating thiol-ene click reaction to crosslink[16]. And synthesis of SMP and HANPs was confirmed by ^{1}H-NMR and raman spectroscopy. Especially, in raman spectroscopy, appearance of wavenumber peak within 2550nm-2650nm means that thiol was synthesized to HANPs[17] (**Fig. 2**). Since H-SMP has some segments that does not exist in SMP, we confirmed differences in mechanical and thermal properties (**Fig. 3**). Degree of crosslinking determined to confirm whether crosslinking occurs effectively even in the presence of HANPs and the result didn't have differences between SMP and H-SMP (**Fig. 3-a**). Also, DSC examined thermal properties of SMP and H-SMP and Tc, Tm and Xc decreased in the presence of HANPs. Because HANPs is a ceramic that has high crystallinity and Tm, after the polymer chains of SMP became amorphous state at high temperature($\geq$Tm), when temperature decreased ($\leq$Tc), the region of HANPs that maintain crystalline structure acts as a nucleating agent, allowing the crystallization to occur more rapidly, leading to an increase or decrease in the Tc and Tm values, respectively (**Fig. 3-b**). And DMA and UTM determined young's and

compressive modulus of SMP and H-SMP. Since hydroxyapatite is a ceramic and it has high mechanical strength, H-SMP has higher young's modulus and compressive modulus (**Fig 3-c,d**). Hence, the presence of HANPs in SMP polymer chains makes enhancement in mechanical and thermal properties.

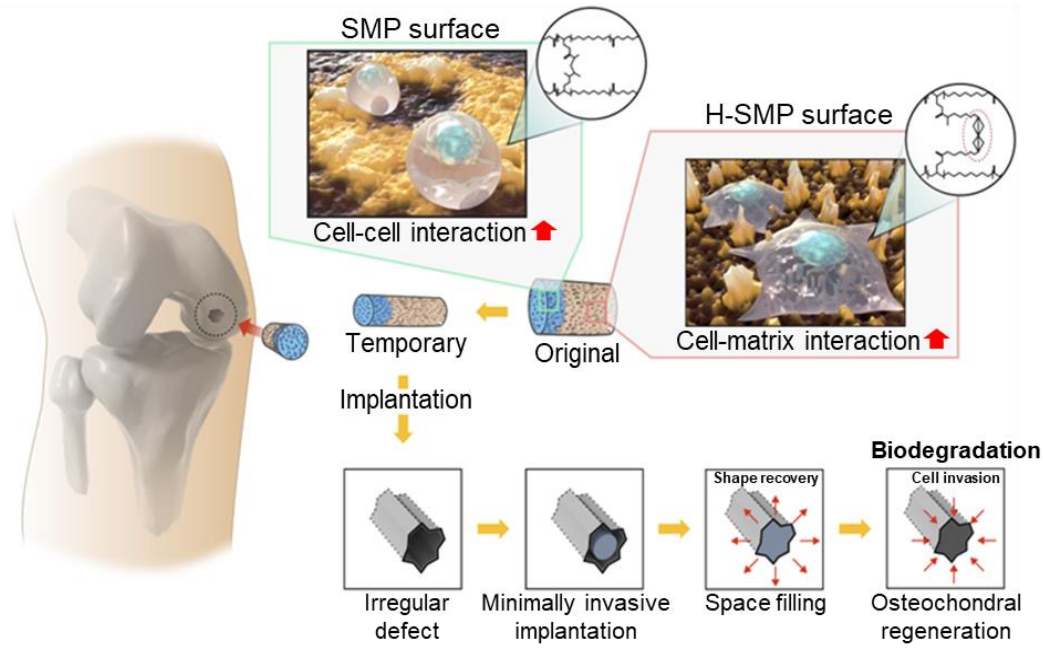

Figure 1. Osteochondral regeneration procedure of biodegradable shape memory polymer scaffold through cell-surface interaction.

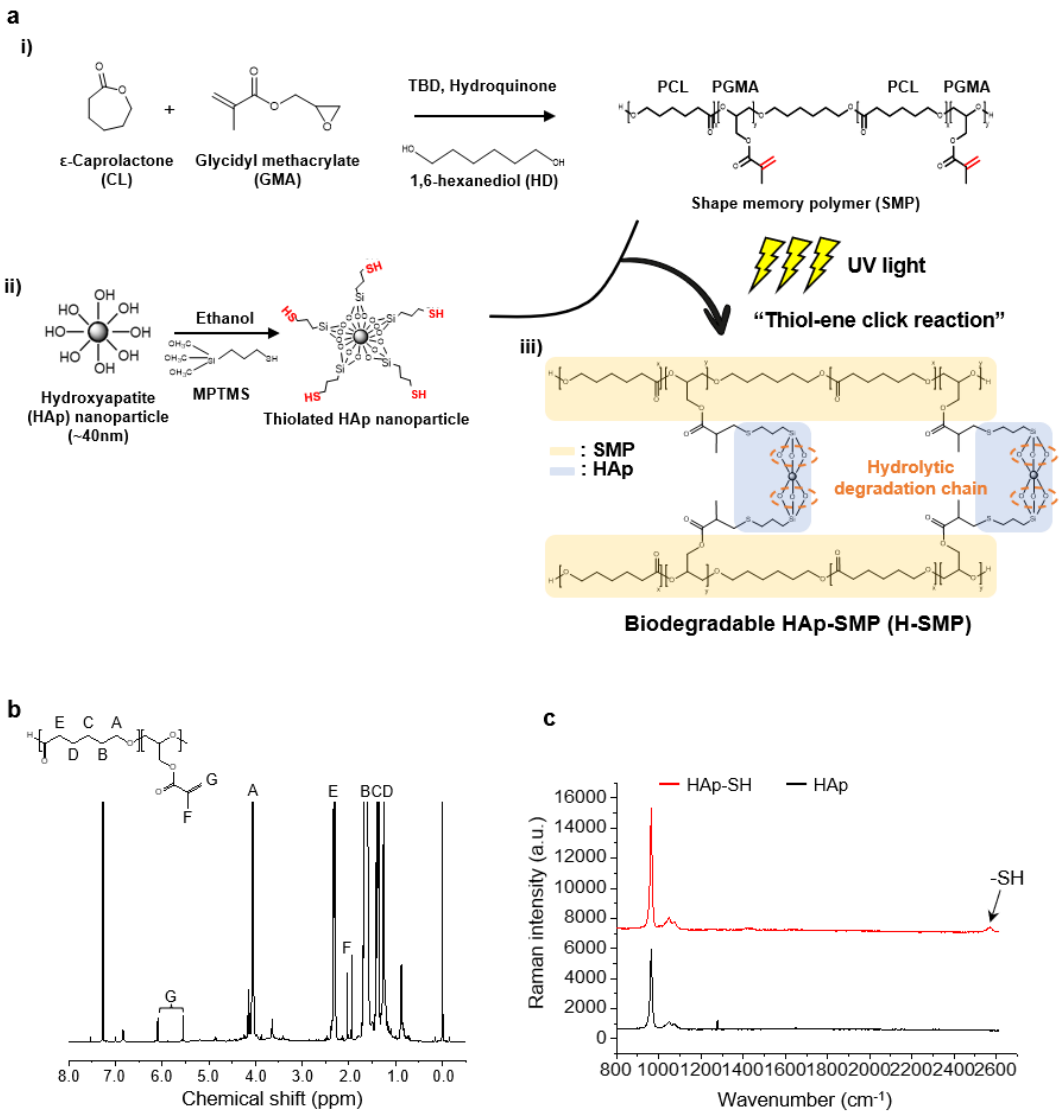

Figure 2. Synthesis process of Shape memory polymer and thiol-modified HANPs and crosslinking between them are shown (a) in schematic. And synthesis of SMP and HANPs was confirmed by (b) H-NMR and (c) raman spectroscopy.

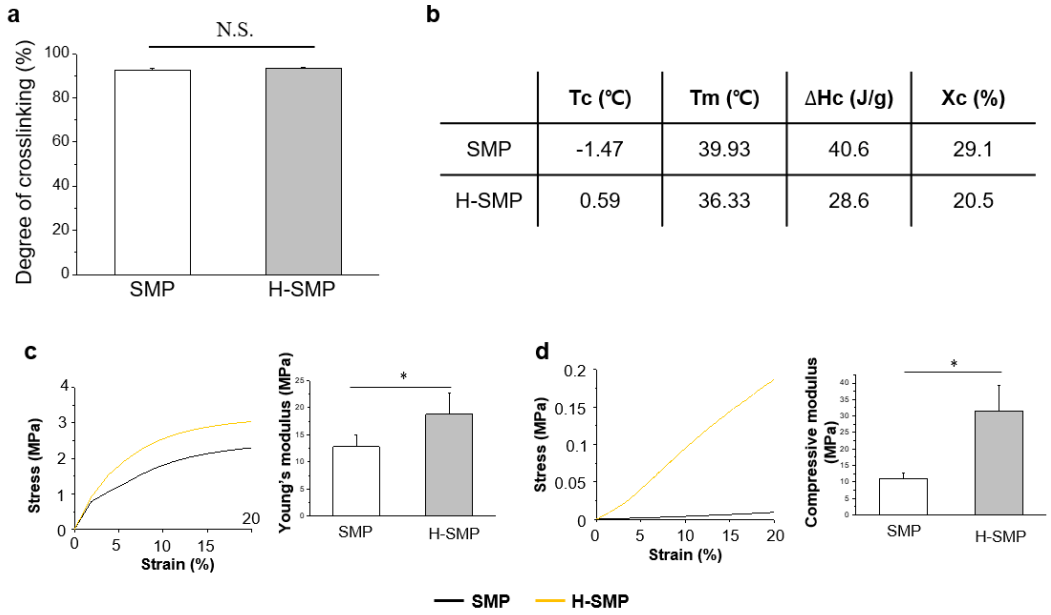

	Tc (℃)	Tm (℃)	ΔHc (J/g)	Xc (%)
SMP	-1.47	39.93	40.6	29.1
H-SMP	0.59	36.33	28.6	20.5

Figure 3. Mechanical and thermal properties of SMP and H-SMP. We confirmed the (a) degree of crosslinking by measuring the weight of the film after immersing it in 1-Methyl-2-pyrrolidinone (NMP) after the crosslinking. And (b) thermal properties of SMP and H-SMP are determined by differential scanning calorimetry (DSC) (Tc: Temperature of crystallization, Tm: Melting temperature, ΔHc: Heat of crystallization, Xc: Degree of crystallization). Dynamic mechanical analysis (DMA) and Universal testing machine (UTM) determined confirmed (c) young's and (d) compressive modulus of SMP and H-SMP films and scaffolds. All data are shown as the mean ± S.D (n=3~5). *$p < 0.05$, **$p < 0.01$, and ***$p < 0.001$ between lined groups.

2. Surface analysis of SMP and H-SMP

Since HANPs act as a nucleating agent with forming crystalline structure[18-20], clustering of crystals occurs around HANPs (“Crystal-packing”). To confirm crystal structures of SMP and H-SMP in 2D and 3D, polarized optical microscopy (POM) and atomic force microscopy (AFM) were used. In 2D crystal structure images, spherulite structure SMP exhibits the characteristic spherulite structure of semi-crystalline polymers[21] and H-SMP shows that the crystals do not have a consistent shape and are irregularly clustered as opaque formations. As evident from the 3D surface topography, SMP exhibits spherulite structure, while in H-SMP, one can observe irregularly clustered crystalline formations (**Fig. 4-a,b**). Furthermore, as crystals grow, clustered crystals induce a concentrated height distribution and high stiffness and roughness in H-SMP. This is because the crystalline structure provides strength, and as a result, the region with densely packed crystals stimulates increased stiffness. Obviously, there is a large variation in height, the surface experiences significant changes in elevation, leading to an increase in roughness. In SMP, regular spherulite structure induces uniform height distribution and lower stiffness and roughness compared to H-SMP. Hence, crystal packing induced by HANPs triggers irregular height distribution, higher stiffness and roughness then SMP (**Fig. 4-c,d,e**). To determine that HANPs were the factors inducing the crystal-packing phenomenon, we conducted surface composition analysis using X-ray diffraction (XRD) and Scanning electron microscope (SEM). In XRD, sharp crystalline peaks in hydroxyapatite were shown in H-SMP compared to SMP (**Fig. 4-f**). Also, SEM images show the cross-section of the film, and by examining the composition of the

cross-section, it can be observed that the ratio of HANPs' primary components, Si, P, and Ca, in the cross-section has increased in H-SMP compared to SMP. This suggests that the particles present in H-SMP were generated by HANPs (**Fig. 4-g**).

Effects of surface crystal structure on SMP and H-SMP surfaces by contact angle and cell adhesion analysis (**Fig 5-a,b**). Consequently, cell adhesion was increased on H-SMP surface due to strengthened cell-surface adhesion. To confirm cell-cell interaction and cell-surface adhesion differences between hBMSCs and SMP/H-SMP films, tight junction marker (ZO-1) and focal adhesion marker (Paxillin) were stained on hBMSCs. As a result, cell-cell interaction marker (ZO-1) expression was increased on SMP film, and cell-surface interaction marker (Paxillin) expression was increased on H-SMP film due to different surface properties of SMP films and H-SMP films.

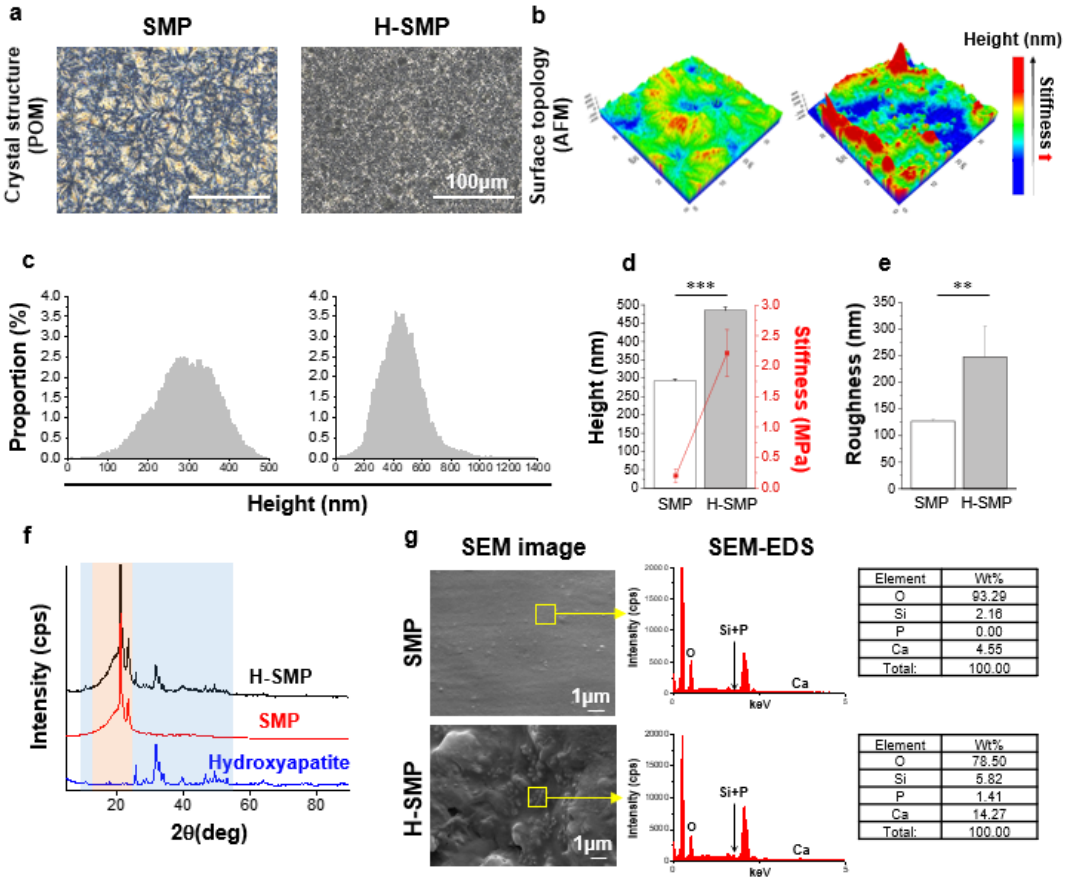

Figure 4. Surface properties of SMP and H-SMP films. Crystal structure of films was confirmed in 2D and 3D. 2D structure was determined by (a) polarized optical microscopy (POM) and 3D structure was confirmed using (b) Atomic force microscopy (AFM). And AFM confirmed (c) height, (d) stiffness, (e) roughness of surface. Also, To confirm whether changes in the surface properties occurred in HANPs, (f) X-ray diffraction (XRD) and (g) SEM were used. All data are shown as the mean ± S.D (n=3~5). *$p < 0.05$, **$p < 0.01$, and ***$p < 0.001$ between lined groups.

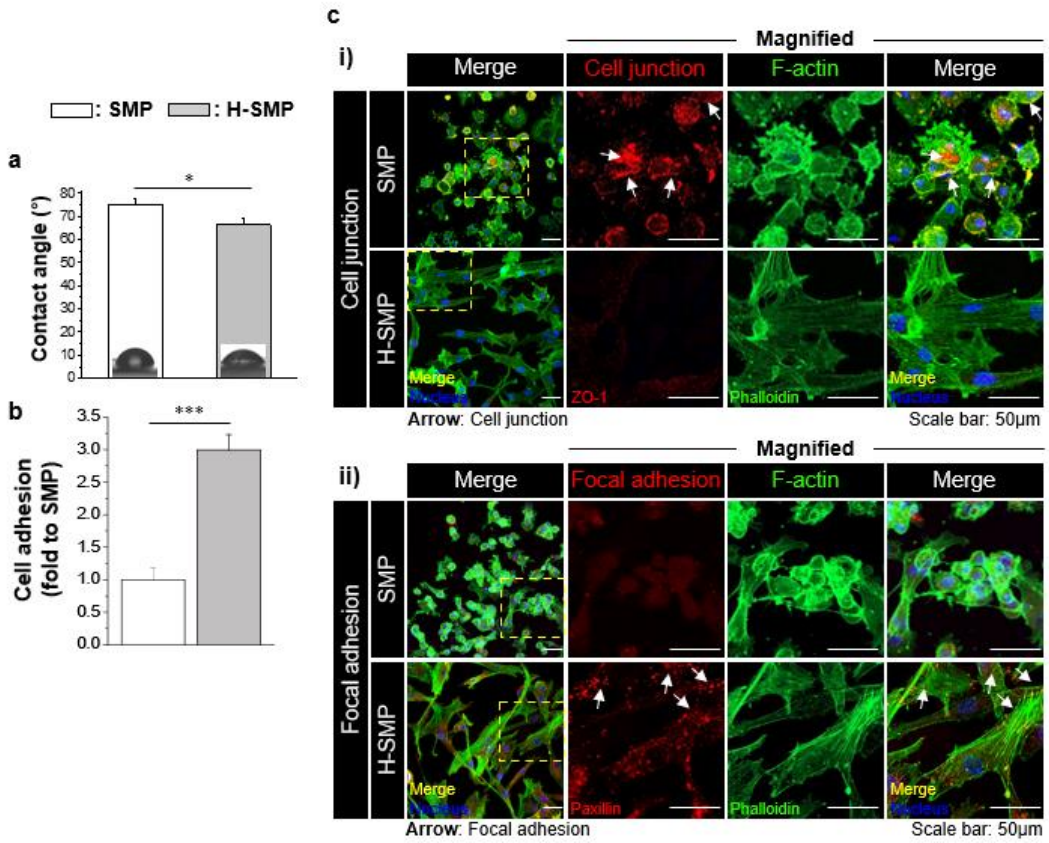

Figure 5. Contact angle analysis and 2D hBMSC mophology differences on SMP and H-SMP surfaces. (a) The contact angle of SMP and H-SMP films was measured in water to investigate differences in hydrophilicity based on roughness. Also, (b) changes in cell adhesion were confirmed using CCK-8 test. To confirm the effects of surface on cell-cell interaction and cell-surface interaction, tight junction marker (ZO-1) and focal adhesion marker (Paxillin) were stained and determined by LSM 980. All data are shown as the mean ± S.D (n=3~5). *p < 0.05, **p < 0.01, and ***p < 0.001 between lined groups.

3. Effects of interactions between 3D hBMSC spheroids and surfaces to differentiation of spheroids

As widely known, spheroids are formed by cell-cell interactions[22-24]. So, as the interaction between spheroids and the surface increases, the interactions among cells within the spheroids become relatively weaker, leading to the dispersion of spherical spheroids (**Fig. 6-a**). To confirm the formation of hBMSC spheroids, they incubated on films in 3 days and actin and nucleus stained (**Fig. 6-b**). The spheroids that incubated on SMP films maintained their spherical morphology. It means that cell-cell interaction didn't distrupt by SMP surfaces. In contrast, the spheroids that incubated on H-SMP films didn't maintain their spherical morphology and cells were sprouted around the spheroids. But, adhesion of spheroids of both films is simillar (**Fig. 6-c**). Hence, the same quantity of spheroids attached to the film surface, but due to the higher interaction between the spheroids attached to the H-SMP film and the surface, they lost their spherical shape. Following the results that SMP induces cell-cell interaction and H-SMP induces cell-surface interaction, We applied this characteristic to cell differentiation, where a high level of interaction between cells leads to aggregation favoring chondrogenesis[25-26], while a high interaction between cells and the surface promotes single-cell spreading, which is advantageous for osteogenesis. To confirm effects of cell-surface interactions on differentiation of spheroids, spheroids incubated chondrogenic/osteogenic differentiation medium. After 3 weeks, immunofluorescence images and quantification shows expression of chondrogenic markers (Col II, Aggrecan;ACAN) increased in SMP and expression of osteogenic markers (Col I, Osteocalcin;OCN) incresed in H-SMP (**Fig. 7-**

a,b). Additionally, the analysis of chondrogenic gene expression (SOX9, ColII, ACAN) and sulfated Glycosaminoglycan showed an increase in SMP, while osteogenic gene expression (RUNX2, Col I, OCN) and calcium deposition showed an increase in H-SMP (**Fig. 7-c,d,e,f**). Therefore, differences in cell-surface interactions affects cell differentiation, especially, chondrogenesis and osteogenesis.

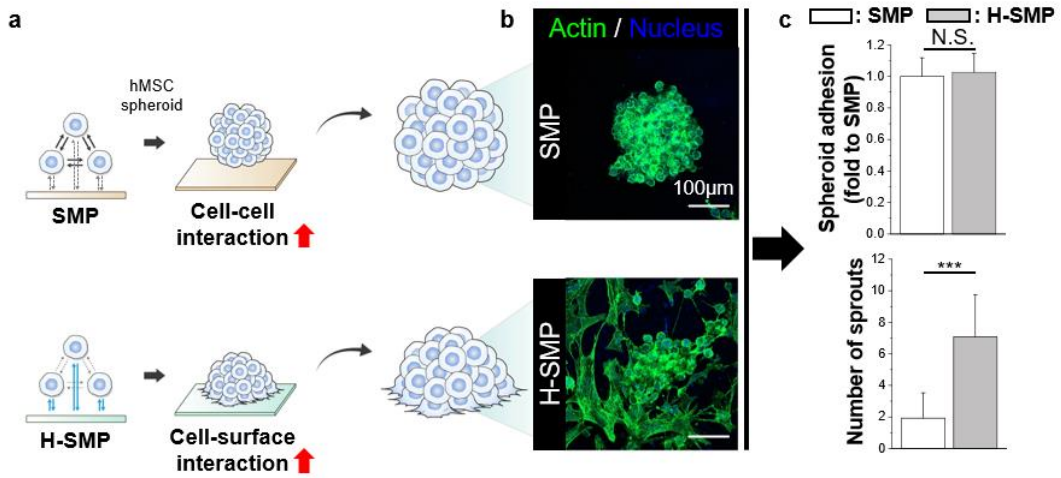

Figure 6. Cell-surface interaction procedure on SMP and H-SMP films with 3D hBMSC spheroids was described as a (a) scheme and (b) immunofluorescene images. To analyze interactions between cells and surfaces, (c) spheroid adhesion was determined by CCK-8 and number of sprouts was investigated by ImageJ. All data are shown as the mean ± S.D (n=5~20). *p < 0.05, **p < 0.01, ***p < 0.001, and N.S.: Not significant. versus SMP or between lined groups.

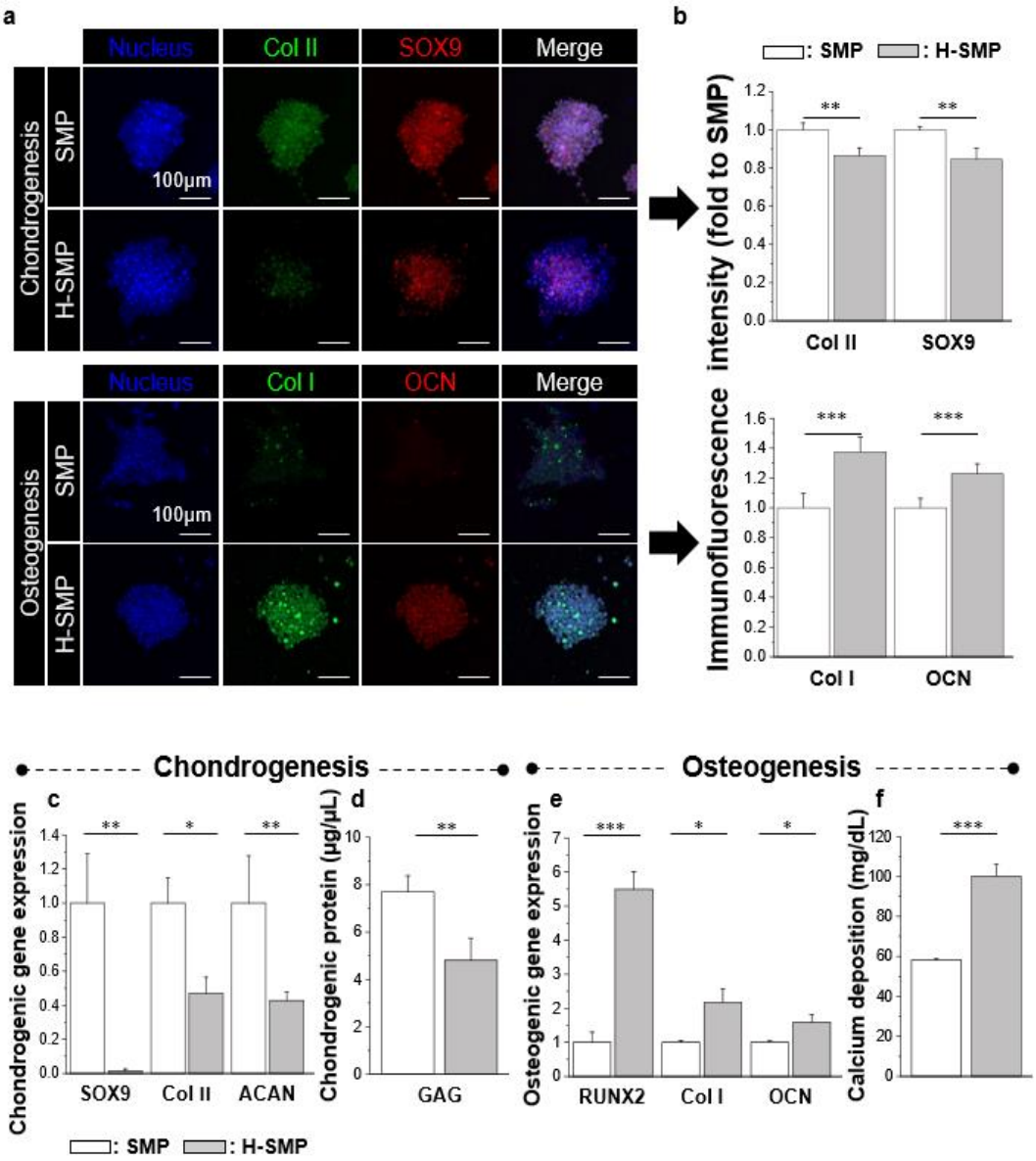

Figure 7. The differentiation differences of hBMSC spheroids based on the interaction between cells and surfaces were confirmed by (a,b) immunofluorescence with LSM980 (Chondrogenesis - Col II: Collagen type II, SOX9/ Osteogenesis – Col I: Collagen type I, OCN: Osteocalcin). Especially, to determine chondrogenic differentiation, (c)

chondrogeinic gene expression (SOX9, Col II, Aggrecan;ACAN) and (d) amount of sulfated Glycosaminoglycan (sGAG) in hBMSC spheorids were measured after 3 weeks of differentiation. Also, osteogenic defferentiation was confirmed by (e) osteogenic gene expression (RUNX2, Col I, OCN) and (f) calcium deposition analysis. All data are shown as the mean ± S.D (n=5). *$p < 0.05$, **$p < 0.01$, and ***$p < 0.001$ versus SMP or between lined groups.

4. Shape memory properties and biodegradability of SMP and H-SMP

Previously, we proved that addition of HANPs to SMP occurs surface modification (e.g. surface tophography, stiffness, roughness). Additionally, films and 3D scaffolds were verified by tensile (tension) and compressive strength, respectively. After films and scaffolds were immersed in hot water (55°C), they were undergone tensile or compressive strength, following fixing of temporary shapes. And then, they were immersed in hot water (40℃) for shape recovery. Both of them were demonstrated that the shape was recovered when they were subjected to various forces (**Fig. 8-a,b**). Also, to apply shape recovery ability for tissue regeneration, scaffolds were implanted to osteochondral defect of rabbit's femur. The temporary shape of scaffold was formed by compressive strength and placed in defect (diameter: 3mm, depth: 3mm) in rabbit. After that, scaffold was immersed in hot water (40°C) for shape recovery (**Fig. 8-c**). To confirm that maintenance of shape recovery ability of H-SMP, it underwent thermomechanical properties over four cycles (N) by dynamic mechanical analysis (DMA) in stress-controlled mode. The melting temperature (Tm) of HANPs is above 1000°C [27-28], so the material's mobility decreases, and it exists in a solid state at the melting temperature of SMP. Therefore, the HANPs crosslinked between the polymer chains of the SMP play a role in holding the chains together, resulting in lower strain in H-SMP than in the melting temperature of SMP. Although decreased strain of H-SMP, its shape recovery ability was proved through stress-controlled thermo-mechanical cycles (**Fig. 8-d**). Also, to confirm that shape-programmed scaffold maintains its temporary

shape at room temperature, original scaffold was immersed in hot water (55°C), adapted to mold with irregularly shaped hole. It didn't recover to original shape at room temperature. And shape filling of scaffold in irregular shape, it was determined in the same manner as before (**Fig. 9-a,b**).

Since HANPs are biodegradable ceramic and improves biodegradability of SMP by crosslinking of HANPs and SMP, enhanced biodegradability of H-SMP was determined both *in vitro* and *in vivo*. First, in vitro degradation test was conducted with scaffolds in 37℃ with shaking and scaffolds were immersed in PBS. After 7,14,28,35 days, scaffolds were obtained, and remaining weight was calculated. Because of improved degradation of H-SMP with hydrolytic degradation, H-SMP scaffolds exhibited approximately 20% higher degradation rate compared to SMP in 35 days (**Fig. 10-a**). In addition to the in vitro degradation test, an in vivo degradation test was also conducted, and it was observed 60 days after insertion into the subcutaneous region of BALB/c mice. The results of in vivo degradation were confirmed with H&E staining and neo tissue invasion area analysis. For tissue regeneration with inserted scaffolds in any tissue, it can occur as the scaffold degrades simultaneously with the infiltration of surrounding tissues, allowing newly formed tissue to fill the void created as the scaffold degrades. In SMP, as the scaffold degradation progressed slowly, the tissue adjacent to the scaffold could not infiltrate inward. In contrast, in the area where H-SMP was inserted, it was observed that a significant portion of the surrounding tissue had infiltrated as the scaffold degraded (**Fig. 10-b,c**). Overall, addition of HANPs to SMP generated improved biodegradability and it is effective to promote tissue regeneration.

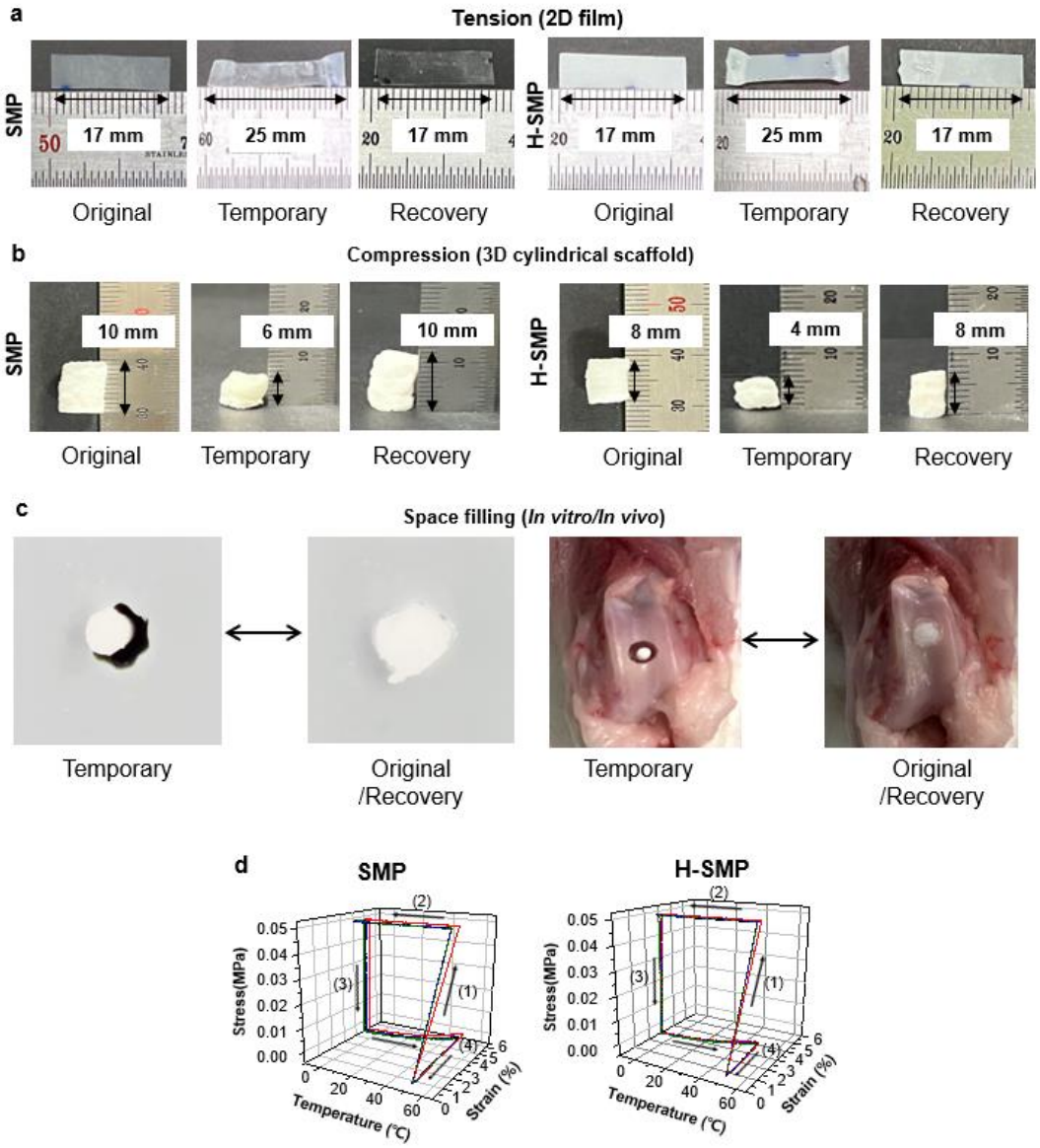

Figure 8. Shape recovery ability of SMP and H-SMP. (a) Tension of SMP/H-SMP films and (b) compression of 3D scaffolds confirmed shape recovery. Also, (c) shape filling ability of 3D scaffolds in the irregular shape (*in vitro*) and the defect of rabbit's femur (*in*

vivo). (d) Four consecutive, stress-controlled thermo-mechanical cycles of SMP and H-SMP represent shape recovery ability.

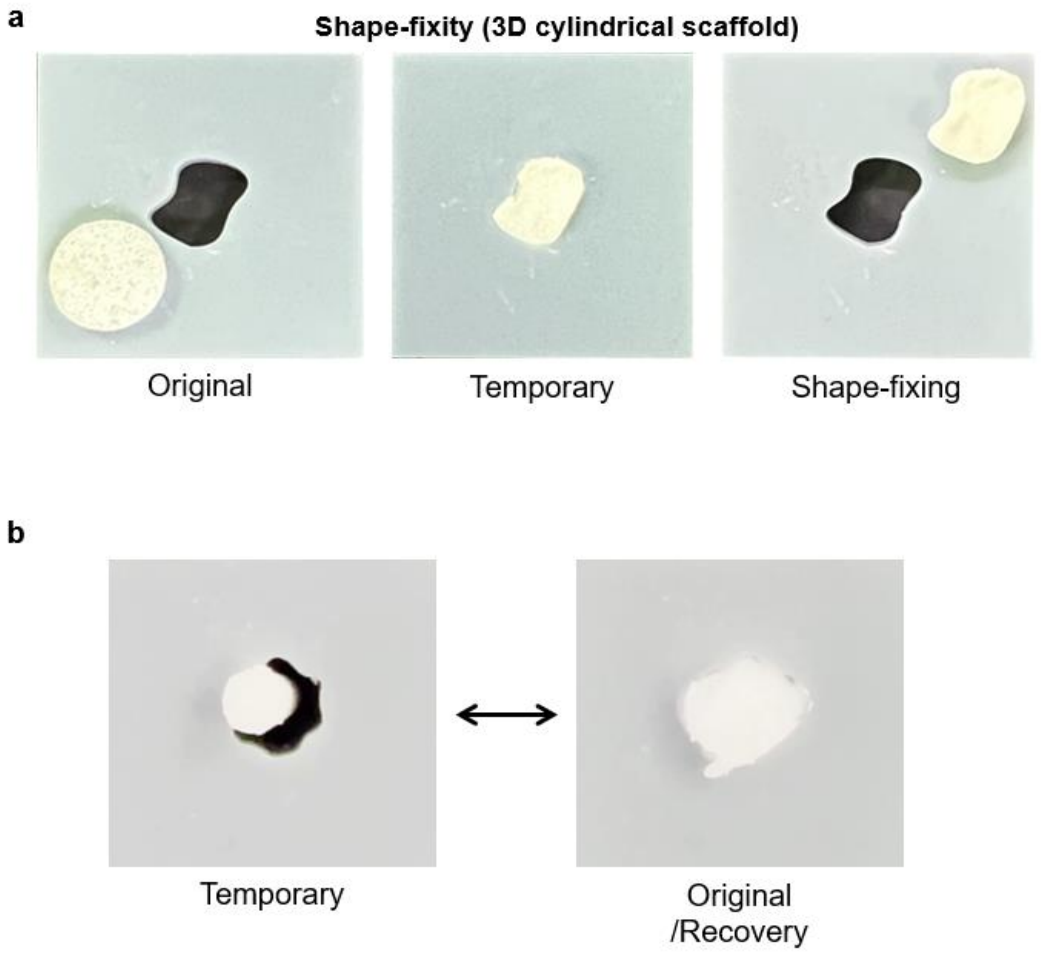

Figure 9. *In vitro* shape fixing and space filling of 3D cylindrical scaffolds in irregular defect. (a) 3D scaffold can maintain temporary shape in RT. And we confirmed that (b) the scaffold, which had been deformed from its original shape, returned to its original form.

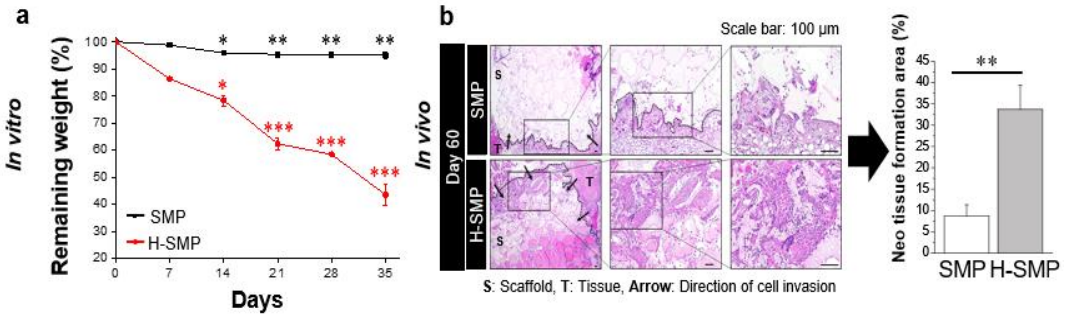

Figure 10. *In vitro* and *in vivo* degradation test of 3D scaffolds. (a) *In vitro* degradation was performed in PBS in pH 6 to mimic *in vivo* environment. In accordance with *in vitro* degradation test, (b) *in vivo* biodegradation test was also performed for 60 days in subcutaneous area of BALB/c's back. Neo tissue invasion area was confirmed with ImageJ, and it shows degree of biodegradation of scaffolds. All data are shown as the mean ± S.D (n=3). *p < 0.05, **p < 0.01, and ***p < 0.001 versus SMP.

5. Effects of biodegradable scaffold with SMP and H-SMP in rat's osteochondral regeneration

Finally, to confirm the effects of biodegradable shape memory polymers in osteochondral regeneration with bilayer scaffolds of SMP and H-SMP. In previous studies, cartilage is a tissue that has limited self-regenerative capacity due to being avascular tissue.[29-32] Regeneration rates are depended on patients' conditions, in general it spends over 6 months. [33] In contrast, the typical time required for bone regeneration is approximately 3 to 6 months. [34] It means that the layer of scaffolds inserted in bone tissue area should degrade and promote bone tissue regeneration, and the layer of scaffolds inserted in cartilage area should endure with low degradation rate until the cartilage tissue is regenerated. So, to apply the importance of the difference in degradation rates of these scaffolds, bilayer scaffolds were created with SMP and H-SMP, positioned simultaneously for the concurrent regeneration of cartilage and bone tissue, with SMP in the cartilage and H-SMP in the bone. As described in a scheme, the shape-programmed bilayer scaffold containing both SMP and H-SMP was inserted in rat's femur (**Fig. 11-a**). To prove that the regenerative effects of the scaffolds were not simply due to the scaffolds filling the defect area, but rather a result of the interaction between the adjacent tissues and the scaffold surface due to the insertion of scaffolds, we inserted not only bilayer scaffolds but also SMP scaffolds in bone tissue are or H-SMP scaffolds in cartilage area, simultaneously. And after creating the defect in rat's femur, we referred to the condition without scaffold insertion as the control. After 8 weeks, animal micro-CT of rat's femur and von-kossa staining were conducted to confirm bone regeneration. Also,

safranin O staining was conducted to confirm cartilage regeneration. In micro-CT images, new bone volume shows that It is evident that bone tissue regeneration is most improved in H-SMP rather than control and SMP. Also, in von-kossa staining, calcium deposition areas (brown) were increased in H-SMP (**Fig. 11-b,c**). In contrast, in safranin O staining, stained cartilage areas were increased in SMP rather than control and H-SMP (**Fig. 11-d**). As mentioned earlier, cartilage is avascular tissue, known for its slow self-regeneration. Typically, cell therapy is primarily used for cartilage regeneration. In this study, we aimed to promote cartilage regeneration using only scaffolds, without the addition of cells. Although it did not achieve the same level of cartilage regeneration as when cells were injected, it resulted in a greater promotion of cartilage regeneration compared to the control or H-SMP, due to the interaction between the tissue and scaffold surfaces. Although 8 weeks was a relatively short duration to achieve complete tissue regeneration, it is evident that there was a relatively improved cartilage regeneration capability within that timeframe. Lastly, to confirm the concurrent regeneration of cartilage and bone tissues, immunofluorescence staining was conducted. For cartilage regeneration confirmation, the expression of Col II and Aggrecan was examined, while for bone regeneration confirmation, the expression of Col I and OCN was assessed. As a result, like the earlier findings, it was observed that cartilage tissue regeneration occurred in the SMP layer, and bone tissue regeneration and biodegradation increased in the H-SMP layer. And it was confirmed with immunofluorescence quantification. (**Fig. 12-a,b**). Overall, addition of HANPs to SMP induces the changes in surface crystal structure, enhanced degradability, and the utilization of surface crystal structure and enhanced

degradability induced improved bone tissue regeneration in osteochondral regeneration. In particular, the differences in crystal structure on the surface had an impact on cell morphology, leading to differences in tissue regeneration through differentiation of cells due to variations in the interaction between the tissue and the surface of SMP and H-SMP scaffolds.

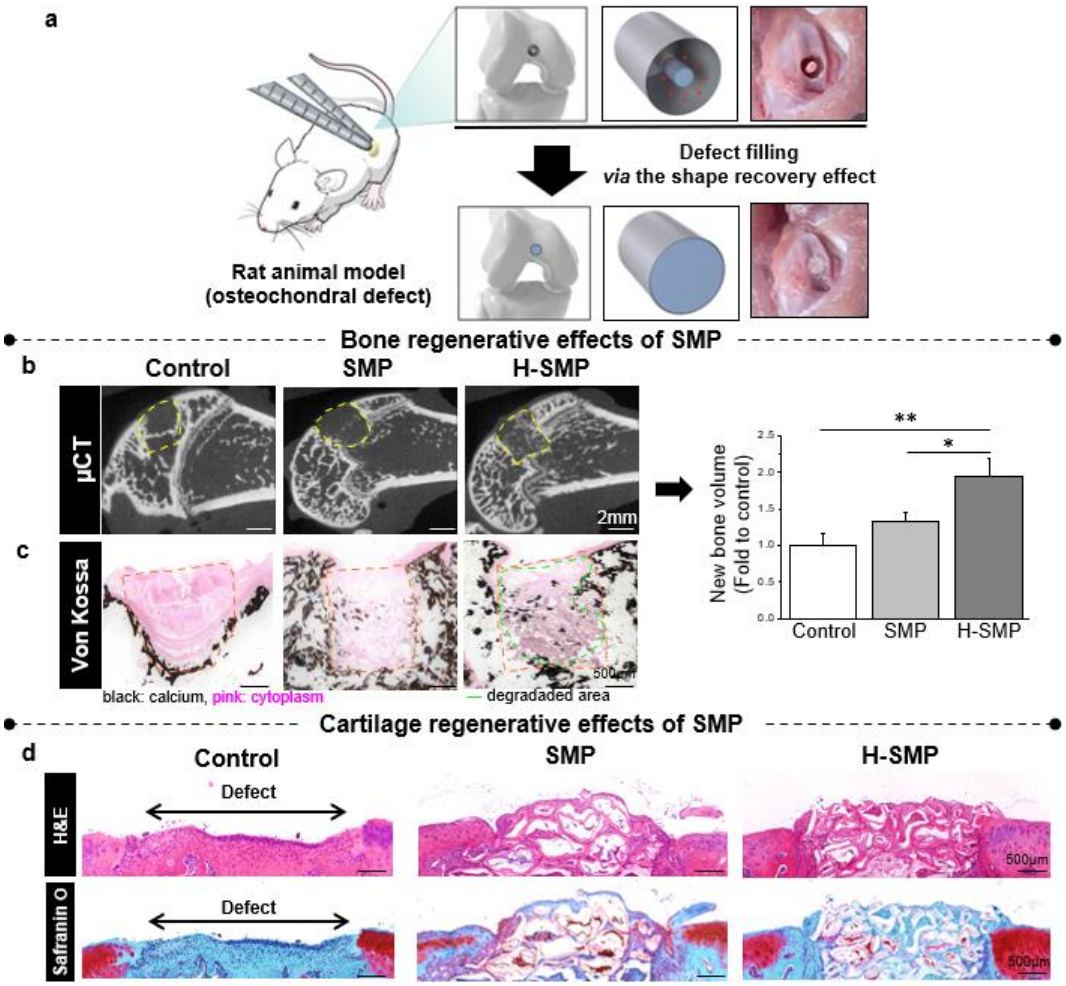

Figure 11. *In vivo* osteochondral regeneration with SMP and H-SMP 3D scaffolds. To confirm cartilage regeneration of SMP scaffolds and bone regeneration of H-SMP scaffolds, osteochondral defect model of rat was used and describes (a) as a scheme and defect filling effects of bilayer scaffolds via temporary shape of bilayer scaffolds. After 8 weeks, bone regeneration of bilayer scaffolds was examined by (b) animal micro CT images and quantification and (c) von kossa staining. Also, (d) H&E and safranin O staining confirmed cartilage regeneration of bilayer scaffolds. All data are shown as the

mean ± S.D (n=5). *$p < 0.05$, **$p < 0.01$, and ***$p < 0.001$ versus control or between lined groups.

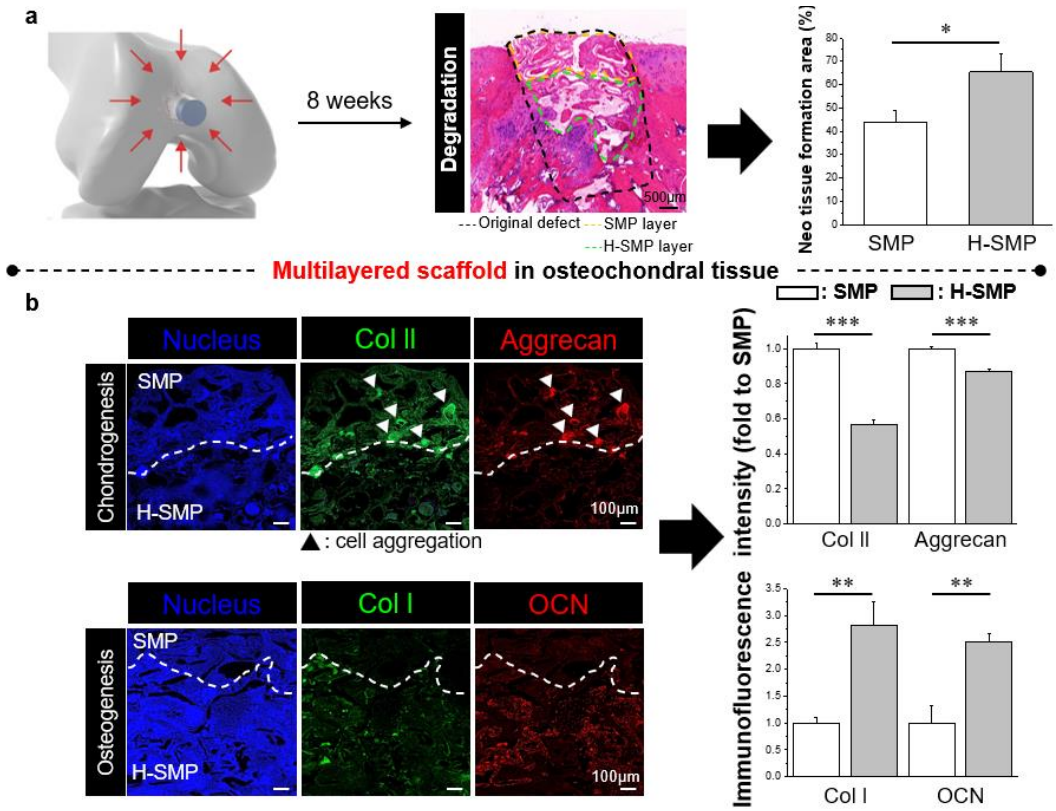

Figure 12. Biodegradation and immunofluorescence staining of rat's osteochondral regeneration model confirmed degradability, cartilage and bone regeneration of SMP/H-SMP bilayer scaffolds with (a) H&E staining of cross-sectioned rat's femur and (b) immunofluorescence images that performed with LSM980. Also, quantification of immunofluorescence intensity with ImageJ. All data are shown as the mean ± S.D (n=5). *p < 0.05, **p < 0.01, and ***p < 0.001 versus SMP.

IV. DISSCUSION

This study presents a new paradigm regarding the interaction between cells and the surface they contact, as well as cell differentiation. Unlike previous studies primarily focusing on how surface stiffness affects cell differentiation, this study aimed to regulate the interaction between cells and the surface through changes in surface crystal structure. In particular, the introduction of highly crystalline materials such as HANPs, when cross-linked with shape-memory polymers, introduced variations in the surface's crystal structure.

Especifically, HANPs were modified with thiol groups on their particle surfaces to facilitate cross-linking with SMP. HANPs are biocompatible and highly degradable ceramics. By cross-linking HANPs with low-degradability SMP, it was expected that the degradability would increase. This effect would be beneficial for tissue regeneration when such polymers are implanted into the body, as tissues can infiltrate into the implanted polymer over time.To confirm this, degradation tests were conducted both in vitro and in vivo, and it was observed that H-SMP exhibited high degradability in both cases. However, due to the inherently low degradability of SMP itself and the relatively low amount of cross-linked HANPs within the overall composition, it was challenging to observe complete degradation within a two-month degradation test. If longer durations or additional factors that could trigger degradation were introduced, it might accelerate the degradation process further. These degradable polymers are expected to play a crucial role in the development of implantable medical devices.

By controlling the surface crystallinity, it is possible to regulate the interaction between the surface and cells. In particular, surface modification with relatively low crystallinity and evenly distributed crystals (SMP) leads to reduced surface-cell interaction, thereby promoting increased cell-cell interactions. Conversely, high crystallinity and irregular crystal arrangements (H-SMP) hinder cell adhesion due to the crystal structure, resulting in enhanced interactions between cells and the surface. These characteristics were applied to promote chondrogenesis through favorable cell-cell interactions and osteogenesis through cell spreading interactions with the surface.

As already known, spheroids are formed in three dimensions through cell aggregation using cell-cell interactions. We aimed to investigate how cell interactions change when spheroids come into contact with the surface of crystalline polymers and examine the differences in chondrogenesis and osteogenesis in response to this. The results revealed that in SMP, there was a higher occurrence of chondrogenesis, while in H-SMP, osteogenesis was more pronounced. In SMP, the relatively uniform arrangement of crystalline structures increased cell-cell interactions, leading to cell aggregation. When spheroids remained in an aggregated state for an extended period, hypoxia conditions were induced from within. This condition is highly favorable for chondrogenesis, as cartilage tissue can undergo differentiation in a hypoxic environment without vascular supply. The induction of hypoxia within long-standing aggregated spheroids is a well-established fact in previous research. Based on this knowledge, it was inferred that SMP is advantageous for chondrogenesis.

Building on the previously discovered findings, we created a platform for simultaneous regeneration of cartilage and bone tissue using SMP and H-SMP bilayer scaffolds. The SMP layer inserted into the cartilage layer demonstrated enhanced cartilage tissue regeneration, while the H-SMP layer inserted into the bone tissue layer exhibited improved bone tissue regeneration. Furthermore, the improved degradability of the H-SMP layer resulted in increased degradation as one moved from the SMP layer to the H-SMP layer, in addition to the enhancement of bone tissue regeneration. Particularly, at the interface between the cartilage tissue layer and the scaffold, cell-surface interactions occurred as cells came into contact, further corroborating the advantage of SMP in chondrogenesis and H-SMP in osteogenesis, as seen in previous results. Based on these research findings, we were able to confirm the effectiveness of controlling surface crystalline structures in shape memory polymers with increased degradability for simultaneous cartilage and bone regeneration.

V. CONCLUSION

H-SMP, a crystalline material with biodegradability, has improved biodegradability by incorporating HANPs and causing crystal aggregation around HANPs, preventing changes in the crystal structure from adhesion between cells and increasing the interaction between cells and surfaces. An increased interaction between cells and surfaces results in a wider cell spreading area, which is advantageous for osteogenesis. Conversely, in SMP, an increased interaction between cells creates a favorable environment for chondrogenesis. By regulating the interaction between surfaces and cells through surface crystal structure control, the ultimate achievement of simultaneous regeneration of bone and cartilage tissue was realized between SMP and H-SMP.

VI. REFERENCE

1. Silvia S. Chen, W.F., Joshua Zimmerberg, Hynda K. Kleinman, Leonid Margolis., Cell-Cell and Cell-Extracellular Matrix Interactions Regulate Embryonic Stem Cell Differentiation. Stem Cells, 2007. 25(3): p. 553-561.
2. Melika Sarem, O.O., Simon Tanaka & V. Prasad Shastri, Cell number in mesenchymal stem cell aggregates dictates cell stiffness and chondrogenesis. Stem Cell Research & Therapy, 2019. 10.
3. Iain Muntz, M.F., Gerjo J V M van Osch and Gijsje H Koenderink, The role of cell–matrix interactions in connective tissue mechanics. Physical Biology, 2022. 19.2: p. 021001.
4. Raluca Tudureanu, I.M.H.-D., Sanda Boca and Ioan Botiz, Insight and Recent Advances into the Role of Topography on the Cell Differentiation and Proliferation on Biopolymeric Surfaces. International Journal of Molecular Sciences, 2022. 23(14): p. 7731.
5. Park Ju Young, L.J.B., Shin Woo Beom, Kang Mi-Lan, Shin Yong Cheol, Son Deok Hyeon, Yi Se Won, Yoon Jeong-Kee, Kim Ji Young, Ko JaeSang, Kim Chang-Soo, Yoon Jin Sook, Sung Hak-Joon Nasolacrimal stent with shape memory as an advanced alternative to silicone products. Acta Biomaterialia, 2020. 101: p. 273-284.
6. Abdullah S. Altorbaq, A.A.K., Xiangning Wen, Ricardo A. Pérez-Camargo, Yunlan Su, Dujin Wang, Alejandro J. Müller, Sanat K. Kumar, Crystallization kinetics and nanoparticle ordering in semicrystalline polymer nanocomposites. Progress in Polymer Science, 2022. 128: p. 101527.

7. Liang, J.L.H., Heterogeneous nucleation and self-nucleation of isotactic polypropylene with addition of nano-ZnO. Journal of Thermal Analysis and Calorimetry, 2021. 146: p. 2115-2126.
8. Wu, B.Z., X. Xu, W. Ren, Y. Leng, H. Liang, L. Zheng, D. Chen, J. Jiang, H., β-Nucleated Polypropylene: Preparation, Nucleating Efficiency, Composite, and Future Prospects. Polymers, 2023. 15.
9. Beh Chong You, C.E.M., Nashrul Fazli Mohd Nasir, Emma Ziezie Mohd Tarmizi, Khor Shing Fhan, Eng Swee Kheng, Mohd Shukry Abdul Majid, Mohd Ridzuan Mohd Jamir, Dielectric and biodegradation properties of biodegradable nano-hydroxyapatite/starch bone scaffold. Journal of Materials Research and Technology, 2022. 18: p. 3215-3226.
10. Pau Turon, L.J.D.V., Carlos Alemán and Jordi Puiggalí, Biodegradable and Biocompatible Systems Based on Hydroxyapatite Nanoparticles. Applied Science, 2017. 7.
11. Shuai Wei, J.-X.M., Lai Xu, Xiao-Song Gu & Xin-Long Ma Biodegradable materials for bone defect repair. Military Medical Research, 2020. 7.
12. Abdelaziz, A.G.N., H.; Abdo, S.M.; Abdalla, M.S.; Amer, A.A.; Abdal-hay, A.; Barhoum, A., A Review of 3D Polymeric Scaffolds for Bone Tissue Engineering: Principles, Fabrication Techniques, Immunomodulatory Roles, and Challenges. Bioengineering, 2023. 10.

13. Jiwon Lim, J.L., Hui-Suk Yun, Hong-In Shin & Eui Kyun Park, Comparison of bone regeneration rate in flat and long bone defects: Calvarial and tibial bone. Tissue Engineering and Regenerative Medicine, 2013. 10: p. 336-340.
14. Rocky S. Tuan, A.F.C.a.B.A.K., Cartilage Regeneration. J Am Acad Orthop Surg, 2016. 21: p. 303-311.
15. Guangming Tiana, G.Z., Shuogui Xub, Tianning Rena, A novel shape memory poly(ε-caprolactone)/hydroxyapatite nanoparticle networks for potential biomedical applications. Journal of Solid State Chemistry, 2019(272): p. 78-86.
16. Bowman, C.E.H.a.C.N., Thiol–Ene Click Chemistry. Angew. Chem. Int. Ed., 2010(49): p. 1540-1573.
17. Paul Bazylewski, R.D.a.G.F., In situ Raman spectroscopy distinguishes between reversible and irreversible thiol modifications in L-cysteine. RSC advances, 2017. 7: p. 2964-2970.
18. H. Deplaine, J.L.G.R., G. Gallego Ferrer, Effect of the content of hydroxyapatite nanoparticles on the properties and bioactivity of poly(l-lactide) – Hybrid membranes. Composites Science and Technology, 2010. 70(13): p. 1805-1812.
19. Ioanna-Georgia I. Athanasoulia, M.N.C., Dimitrios M. Korres and Petroula A. Tarantili, The effect of hydroxyapatite nanoparticles on crystallization and thermomechanical properties of PLLA matrix. Pure Appl. Chem., 2016. 89(1): p. 125-140.

20. Jia Wang, W.Q., Ning Wanga and Li Li, Influence of hydroxyapatite on thermoplastic foaming performance of water-plasticized poly(vinyl alcohol). RSC advances, 2015(103): p. 84578-84586.
21. Chengtao Yu, Q.X., Yongzhong Bao, Guorong Shan and Pengju Pan, Crystalline and Spherulitic Morphology of Polymers Crystallized in Confined Systems. Crystals, 2017. 7(147).
22. Bozidar Djordjevic, C.S.L., Cell-cell interactions in spheroids maintained in suspension. Acta Oncologica, 2005: p. 412-420.
23. Youngbin Cho, S.J.Y., Jiwon Kim, Ung Hyun Ko, Eun Young Park, Jin Seung Choung, Goro Choi, Daehyun Kim, Eunjung Lee, Sung Gap Im, and Jennifer H. Shin, Remodeling of Adhesion Network within Cancer Spheroids via Cell–Polymer Interaction. ACS Biomater. Sci. Eng., 2020: p. 5632-5644.
24. Yu Bin Lee, E.M.K., Hayeon Byun, Hyung-kwan Chang c, Kwanghee Jeong d, Zachary M. Aman d, Yu Suk Choi e, Jungyul Park c, Heungsoo Shin, Engineering spheroids potentiating cell-cell and cell-ECM interactions by self-assembly of stem cell microlayer. Biomaterials, 2018. 165: p. 105-120
25. Glennon-Alty, L., Williams, R., Dixon, S., & Murray, P. (2013). Induction of mesenchymal stem cell chondrogenesis by polyacrylate substrates. Acta biomaterialia, 9(4), 6041–6051.
26. He, H., He, Q., Xu, F., Zhou, Y., Ye, Z., & Tan, W. S. (2019). Dynamic formation of cellular aggregates of chondrocytes and mesenchymal stem cells in spinner flask. Cell proliferation, 52(4), e12587.

27. Roopalakshmi, S., Ravishankar, R., Belaldavar, S., Prasad, R. V., & Phani, A. R. (2017). Investigation of structural and morphological characteristic of hydroxyapatite synthesized by sol-gel process. Materials Today: Proceedings, 4(11), 12026-12031.
28. Shuai, C., Zhou, Y., Yang, Y., Feng, P., Liu, L., He, C., Zhao, M., Yang, S., Gao, C., & Wu, P. (2017). Biodegradation Resistance and Bioactivity of Hydroxyapatite Enhanced Mg-Zn Composites via Selective Laser Melting. Materials (Basel, Switzerland), 10(3), 307.
29. Nossin, Y., Farrell, E., Koevoet, W. J. L. M., Datema, F., Somoza, R. A., Caplan, A. I., & van Osch, G. J. V. M. (2021). The Releasate of Avascular Cartilage Demonstrates Inherent Pro-Angiogenic Properties In Vitro and In Vivo. Cartilage, 13(2_suppl), 559S–570S.
30. Liu, Y., Shah, K. M., & Luo, J. (2021). Strategies for articular cartilage repair and regeneration. Frontiers in Bioengineering and Biotechnology, 9, 770655.
31. Danišovič, L. U., Varga, I., Zamborský, R., & Böhmer, D. (2012). The tissue engineering of articular cartilage: cells, scaffolds and stimulating factors. Experimental biology and medicine, 237(1), 10-17.
32. Iwamoto, M., Ohta, Y., Larmour, C., & Enomoto-Iwamoto, M. (2013). Toward regeneration of articular cartilage. Birth defects research. Part C, Embryo today : reviews, 99(3), 192–202.
33. Tiku, M. L., & Sabaawy, H. E. (2015). Cartilage regeneration for treatment of osteoarthritis: a paradigm for nonsurgical intervention. Therapeutic advances in musculoskeletal disease, 7(3), 76–87.

34. Ansari M. (2019). Bone tissue regeneration: biology, strategies and interface studies. Progress in biomaterials, 8(4), 223–237.

ABSTRACT (IN KOREAN)

생분해성 형상기억고분자: 표면 결정 구조의 골연골 재생에서의 효과

<지도교수 성학준>

연세대학교 대학원 의료기기산업학과

박수지

조직 공학 및 재생 의학 분야에서는 뼈와 연골 조직을 모두 복구하는 복잡하고 역동적인 요구를 해결할 수 있는 혁신적인 전략에 대한 요구가 증가하고 있다. 골재생 및 연골재생 환경을 모방하기 위해 세포가 부착되는 고분자 표면의 결정성은 세포와 표면 사이의 상호 작용을 조절하기 때문에 중요하다. 상호 작용을 제어하기 위해 형상기억 고분자(SMP)와 thiol 반응기 기능화 하이드록시아파타이트 나노입자(HANP)는 결합되고 HANP 의 결정 구조는 핵생성제로 작용하며 HANP 입자 주위의 결정의 응집을 자극한다. 결정이 성장함에 따라 세포 간의 상호 작용이 방해받으며 동시에 세포와 표면 간의 상호 작용이 골재생을 위해 강화되는 반면 대조적으로 SMP 표면은 연골생성을 위해 상대적으로 세포-세포 상호 작용을 유도한다. 그리고 HANP 결합 SMP (H-SMP)는 SMP 에 비해 증가된 생분해성을 나타낸다. H-SMP 의

향상된 생분해성은 뼈 재생 속도에 적합한 반면 SMP 의 상대적으로 느린 분해는 연골 재생 속도에 적합하다. 결과적으로 생분해성 SMP 및 H-SMP 구배 3D 다공성 지지체는 쥐의 골연골 결손 모델에서 뼈와 연골의 동시 재생을 나타낸다.

핵심되는 말: 표면 결정 구조, 생분해성, 형상기억고분자, 골연골재생.